High-performance aqueous sodium-ion/sulfur battery using elemental sulfur

Mukesh Kumar
Indian Institute of Technology Ropar
Neha Thakur
Indian Institute of Technology Ropar
Ankur Bordoloi
Indian Institute of Petroleum
Ashok Yadav
Bhabha Atomic Research Centre
Shambhunath Jha
Bhabha Atomic Research Centre
Dibyendu Bhattacharyya
Bhabha Atomic Research Centrea https://orcid.org/0000-0002-1657-1858
Debaprasad Mandal
Indian Institute of Technology Ropar https://orcid.org/0000-0003-4701-543X
Tharamani C. Nagaiah (tharamani@iitrpr.ac.in)
Indian Institute of Technology Ropar

Article

Keywords: aqueous sodium-ion batteries (ARSIBs), elemental sulfur, Energy storage

Posted Date: April 16th, 2021

DOI: https://doi.org/10.21203/rs.3.rs-382906/v1

High-performance aqueous sodium-ion/sulfur battery using elemental sulfur

Abstract:

Despite a promising outlook, the large-scale application of aqueous rechargeable sodium-ion batteries (ARSIBs) was impeded due to low-capacity electrode materials. Herein we report a high capacity elemental sulfur-based anode (S@NiVP/Pi-NCS) for aqueous rechargeable sodium ion-sulfur batteries using 70 % of elemental sulfur which deliver an outstanding capacity of 826 mA h g^{-1} at 0.5 C with an excellent cycling stability even at 10 C and a negligible capacity decay with 0.03 % sulfur loss per cycle even after 400 cycles. *In-situ* spectro-electrochemical analysis confirms good anchoring ability of the anode and a faster redox kinetics of polysulfide conversion. The chemical interaction with vanadium provides faster redox kinetics of polysulfide conversion and efficient anchoring as revealed by XPS and was further supported by XANES and EXAFS studies wherein the distortion at the V site and overlapping electronic states in NiVP/Pi catalyst was observed. Further, full cell battery using S@NiVP/Pi-NCS anode and $Na_{0.44}MnO_2$ cathode demonstrates an excellent initial capacity of 705 mA h g^{-1} based on S loading and 91.7 mAh g^{-1} w.r.t. total electrode weight at 0.5 C with 91 % of capacity retention after 400 cycles and two full cells connected in series able to power LED demonstrate its practical application.

Introduction:

The development of safe, cost-effective, and high energy density batteries is a grand challenge of the 21st century for large storage applications such as electric vehicles and other grid storage applications.[1,2] Despite the Lithium-ion batteries (LiBs) are well established but stumbles upon several challenges, prominently moderate energy density (<400 Wh kg^{-1}), highly flammable non-aqueous electrolyte, and ubiquitous safety concerns associated with the dendritic growth of Li in highly inflammable ether-based electrolytes.[3,4] Besides, lithium scarcity and non-uniform geographical distribution render it's challenging to meet the immensely growing demand for energy in the near future.[5] In recent years, environmental generous aqueous rechargeable sodium-ion battery (ARSIB) able to draw significant research curiosity due to low cost and high safety compared to organic counterparts and deemed as promising and economical energy storage technology for the future.[6] More importantly, aqueous electrolyte alluring towards lower viscosity and high conductivity allows ARSIB batteries to operate at high current density compared to the organic electrolyte.[7,8] Besides safety, manufacturing costs can be reduced significantly due to the elimination of firm inert conditions and drying assembly lines.[9] Despite many benefits of the aqueous system, unfortunately, grid application of ABs is limited by unsatisfactory energy density arises due to limited operating potential window of 1.23 V because of oxygen and hydrogen gas evolution (OER and HER) occurs due to water electrolysis. [10,11]

Despite potential limitations, a significant amount of stable cathode materials, including a metal oxide,[12-14] polyanion,[15,16] and Prussian blue analogues,[6,17-20] have been reported. However, the development of anode material is challenged by poor stability, competitive HER and low capacity, leading to decreased energy density and poor cycling performance.[21,22] Hence, the development of high capacity anode material is of utmost importance. Sulfur, is considered to be a promising electrode material with high theoretical capacity (1675 mA h g^{-1}), high energy density (2600 Wh Kg^{-1}), low cost, earth abundance, and environment benign.[23] The inclusion of both earth-abundant materials such as sulfur and sodium along with environment benign aqueous electrolyte would be a game-changing strategy. Thus, creates safe, cost effective and high-rate

performance cell chemistry without Li-metal and flammable electrolyte and make the aqueous rechargeable Na-ion/sulfur battery a prudent choice for next-generation energy storage. But the most critical challenge in the aqueous sulfur battery is the polysulfide dissolution during the discharge process, similar to the organic system.[24] However, in aqueous electrolyte, the polysulfides react with water to form HS^- and H_2S gas, leading to the loss of active sulfur and capacity decay upon battery cycling.[25]

Although non-aqueous sulfur based batteries progressively getting significant attention from last one decade, only three reports on sulfur-based anode materials such as S@PPy[26], MWCNTs@S@PPy and sulfur- ketjen black have been reported in the recent past for aqueous electrolyte.[25,27] More importantly, for Na-ion/S battery there is only one report where dissolved polysulfide was used as an anode in ARSIBs.[28] The key catalyst requirement for sulfur based batteries is that the catalyst should anchor the polysulfide and enable accelerated polysulfide redox kinetics. Transition metal phosphide/phosphate have been extensively used in various electrocatalytic applications due to its high conductivity compared to other polar transition metal oxide and sulfide, and expected to accelerate polysulfide kinetics by strong chemical interaction. Herein we have explored the combination of nickel vanadium phosphide/phosphate (NiVP/Pi) and nitrogen containing carbon spheres (NCS) with 70% elemental sulfur (S@NiVP/Pi-NCS) as anode for ARSIBs. The main prospect of the present study was to develop highly conductive anode that confines polysulfide within electrode to inhibit H_2S formation and accelerate the polysulfide redox kinetics. The proposed S@NiVP/Pi-NCS reported to be the first entrant as anode for ARSIBs, demonstrating an unprecedented capacity of 826 mA h g^{-1} at 0.5 C with an excellent cycling performance over 400 cycles at a very high C-rate of 10 C which discloses very low capacity fading of 0.03 % per cycle. A full cell battery with $Na_{0.44}MnO_2$ cathode demonstrate, an initial capacity of 705 mA h g^{-1} w.r.t sulfur loading and 91.71 mA h g^{-1} w.r.t total electrode weight at 0.5 C with a very high-capacity retention of 91 % even after 400 cycles. Practical application was further shown by lightening a LED powered by two charged full cells connected in series.

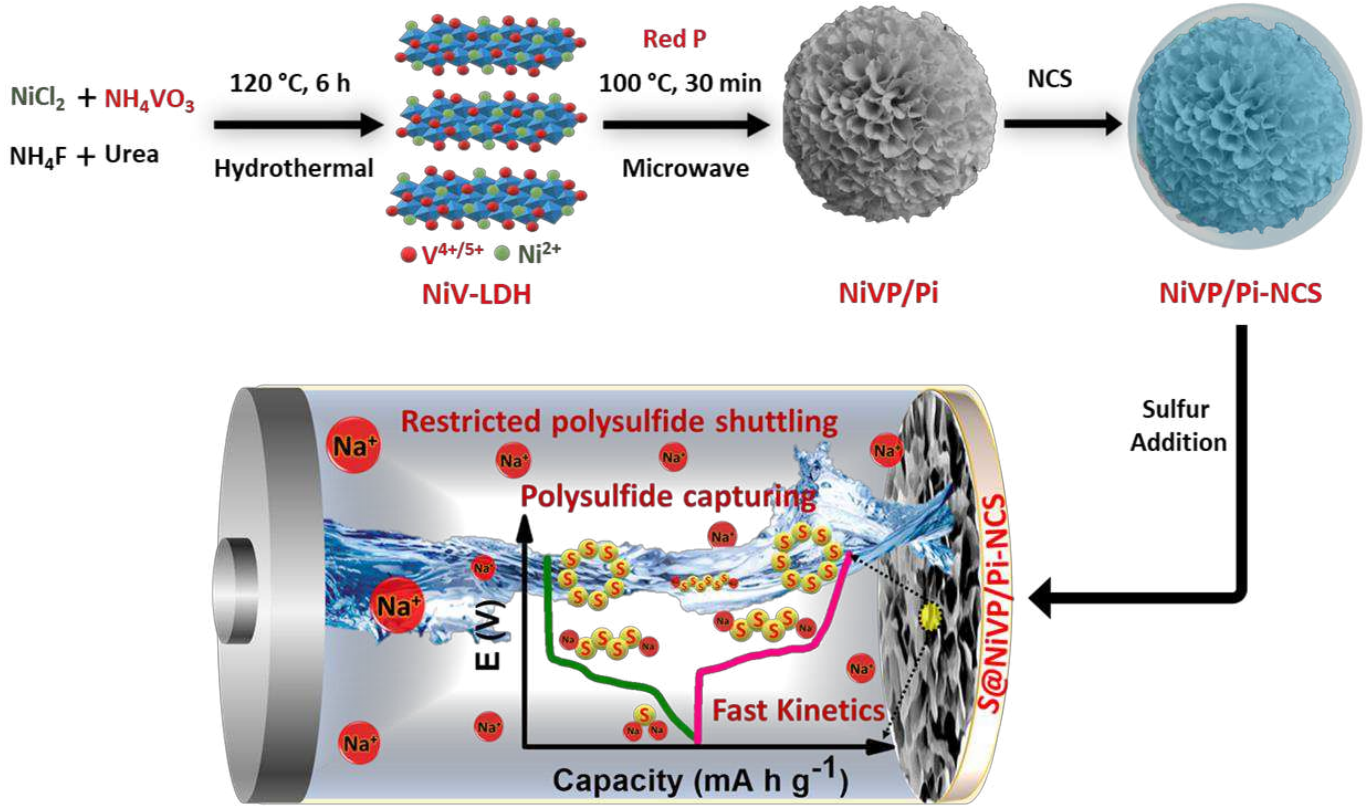

Scheme 1. Interaction of polysulfide @ anode. The synthetic protocol of NiVP/Pi-NCS and redox conversion of polysulfide at S@NiVP/Pi-NCS anode in aqueous Na-ion/S battery.

Result and Discussion:

The NiVP/Pi microsphere synthesis involves a facile two-step approach, initially hydrothermal treatment of nickel chloride and ammonium metavanadate salts with urea to form nickel vanadium layered double hydroxide (NiV-LDH) followed by low-temperature (100 °C) microwave-assisted phosphidation with red phosphorous [synthesis detailed in supporting information, (SI)]. The nitrogen-containing carbon spheres (NCS) were synthesized by employing a soft templating approach using Triton X-100 following the reported procedure (detailed in Supplementary).[29] The proposed anode S@NiVP/Pi-NCS was prepared by physically grinding 1:1 ratio of NiVP/Pi and NCS followed by sulfur incorporation by melt diffusion @ 155 °C for 12 h and was further mixed with PVDF binder to give 25:70:5 wt.% of NiVP/Pi-NCS, sulfur,

and PVDF respectively (detailed in experimental section). Similarly, S@NiVP/Pi anode was synthesized with the same sulfur content (detailed in Supplementary) for control experiments.

The estimation by thermogravimetric analysis (TGA) confirms 68 % of sulfur in the developed anode S@NiVP/Pi-NCS, indicating the successful incorporation of sulfur (Supplementary Fig. 1). The synthesized NiVP/Pi by scanning electron microscopy (SEM, Fig. 1a) reveals the microsphere morphology resulted from several ultrathin nanosheets organized almost vertical to the surface that are crosslinking together resulting in a multilayer 3D network structure of spheres. These were further supported by transmission electron microscopy (TEM) and high-resolution TEM (HR-TEM) techniques (Figs. 1b-1c). Further, the scanning TEM (STEM) image and corresponding element dot mapping discloses the homogeneous distribution and coexistence of Ni, V, O and P within the spheres (Figs. 1d-1h). The selected area electron diffraction (SAED) pattern in Supplementary Fig. 2 shows the lower crystallinity due to the nanosheet structure. The powder X-ray diffraction (PXRD) pattern (Supplementary Fig. 3) resembled with reported NiV-LDH, more importantly after phosphidation, an additional peaks due to $NiPO_4$ and NiP was appeared along with NiV-LDH signifying the successful formation of nickel vanadium phosphide/phosphate designated as NiVP/Pi.[30,31] The XRD pattern of NCS illustrates an amorphous nature with two broad peaks, one at 26° corresponding to (002) plane and the other at 43° for (100) plane signifying the presence of sp^2 carbon network.[29] While, after mixing with NCS (NiVP/Pi-NCS), the disappearance of the peaks w.r.t NiVP/Pi and a slight shift in the graphitic carbon (24.8°) was observed, signifying the casting of NCS over NiVP/Pi, which was further supported by SEM images (Supplementary Fig. 4). More importantly, after incorporation of sulfur, sharp, intense multiple peaks indexed to orthorhombic sulfur was observed with lower intensity in S@NiVP/Pi-NCS compared to pristine sulfur, signifying the successful incorporation of sulfur (Supplementary Fig. 5).[32]

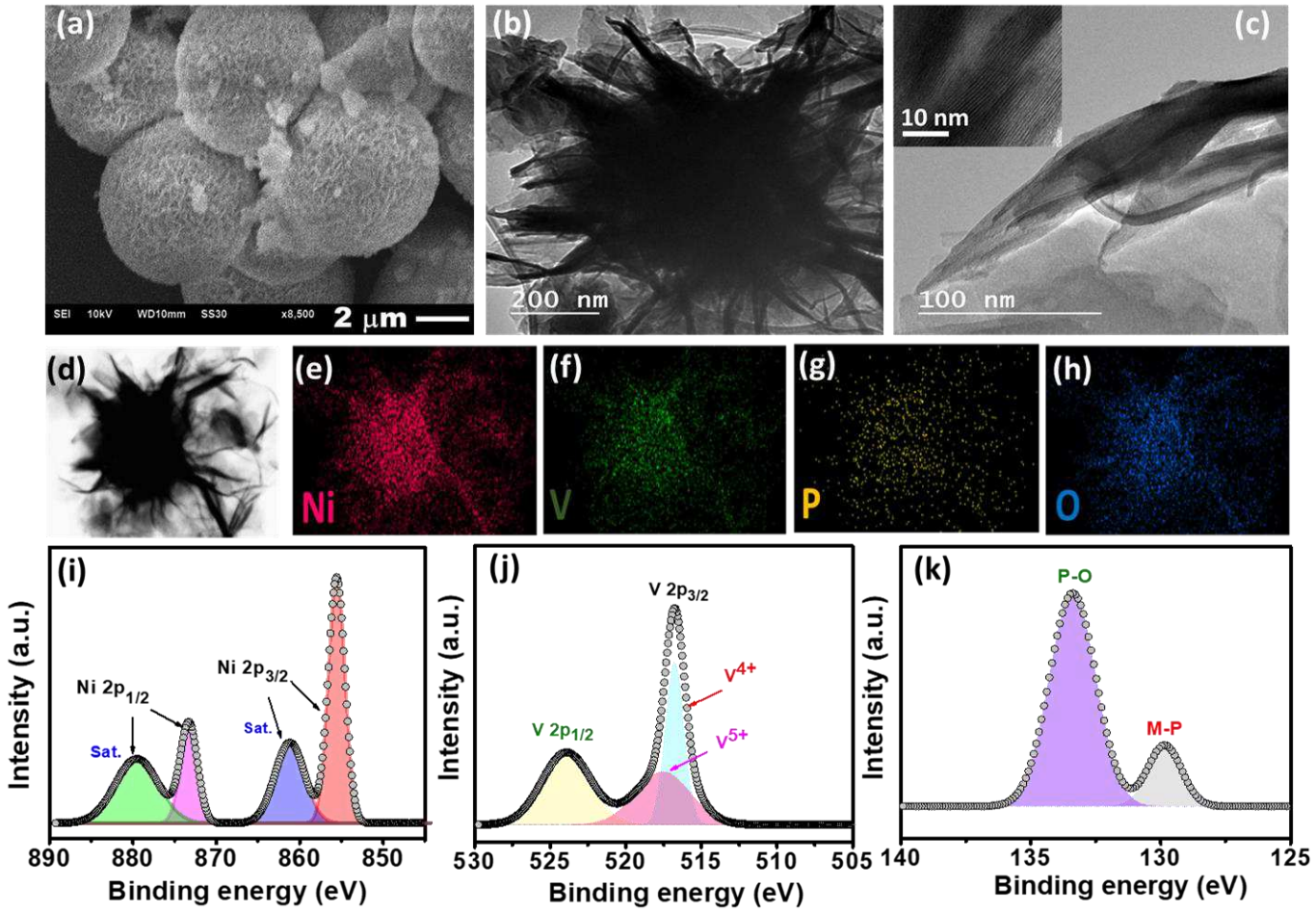

Fig. 1. Microstructure, morphology characteristics and XPS of NiVP/Pi. (a) SEM, (b) TEM and (c) HTEM images of NiVP/Pi, (d) STEM image of NiVP/Pi and corresponding EDS elemental dot mapping images of (e) nickel, (f) vanadium, (g) phosphorous and (h) oxygen, deconvoluted XP spectra of (i) Ni 2p, (j) V 2p, and (k) P 2p of NiVP/Pi.

The oxidation state of NiVP/Pi was analyzed by X-ray photoelectron spectroscopy (XPS). The XP survey spectrum confirms the presence of Ni, V, P, O elements, and no impurities were present (Supplementary Fig. 6). As shown in Fig. 1i, the deconvoluted Ni 2p XP spectrum of as-prepared NiVP/Pi exhibits two peaks corresponds to Ni $2p_{1/2}$ and Ni $2p_{3/2}$ at a binding energy of 873.3 eV and 855.5 eV respectively, which are separated by 17.6 eV along with satellite peaks at 879.4 eV and 861.1 eV attributed to Ni^{2+}. Similarly, the deconvoluted V 2p XP spectrum (Fig. 1j)

reveals V $2p_{1/2}$ and V $2p_{3/2}$ due to spin-orbit coupling and the peak of V $2p_{3/2}$ can be fitted into two constituent peaks corresponding to V^{4+} (516.7 eV), V^{5+} (517.5 eV).[30] The P 2p XP spectrum shows two peaks, one at higher binding energy (133.4 eV) corresponds to phosphate species while low intense peak at 129.8 eV attributed to metal phosphide (Fig. 1k). The O 1s XP spectrum shows two peaks located at 530.7 eV, 531.7 eV which can be assigned to O^{2-}, OH^{-}, respectively (Supplementary Fig. 6b).

Besides, the electronic structure and electronic environment of the NiVP/Pi catalyst were studied using X-ray absorption near edge structure (XANES) and extended X-ray absorption fine structure (EXAFS) techniques. The normalized XANES spectrum of NiVP/Pi at Ni K-edge is shown in Fig. 2a along with standards Ni foil, and NiO. The absorption edge position in XANES spectrum corresponds to the oxidation state of the absorbing atom and it shifts towards higher energy with increasing oxidation state. Absorption edge position of NiVP/Pi clearly coincides with NiO indicates +2 oxidation state of Ni-ions, however the EXAFS oscillations (Fig. 2b) clearly indicate different structure compared to NiO. The pre-edge peak can also be seen in NiVP/Pi with relatively less amplitude compared to NiO which is originated from the transition of 1s electron into higher level empty d states in transition metals due to hybridization.

The normalized XANES spectrum of NiVP/Pi at V K-edge is shown in Fig. 2c along with V foil standard and V_2O_5, $VOPO_4$, VO_2 references. As observed from Fig. 2c, the absorption edge of NiVP/Pi is located between $VOPO_4$, V_2O_5 and VO_2, indicating a mixed oxidation state of +5 and +4, which are consistent with XPS results (Fig. 1j). More importantly, a relatively high intense pre-edge peak (5469 eV) in the V K-edge XANES obtained from 1s to 3d transition suggesting a strong hybridization and a higher degree of distortion at the V sites due to Ni incorporation in NiVP/Pi.

The Fourier-transform (FT) EXAFS spectrum at Ni K-edge and V K-edge were also recorded to investigate the structure of NiVP/Pi at the atomic level. The spectrum in Fig. 2d exhibited two projecting coordination peaks at 1.56 Å and 2.7 Å that are ascribed to the Ni-O peak and Ni-Ni/V peak.[33,34] The FT-EXAFS

spectrum of NiVP/Pi at V K-edge in Fig. 2e shows the first peak at 1.52 Å of V–O bond which is a slightly lower bond distance compared to the standard samples V_2O_5, $VOPO_4$, and VO_2. Two peaks between 2.0-3.5 Å is contribution of V-Ni and V-V coordination at 2.56 Å and 3.36 Å respectively.

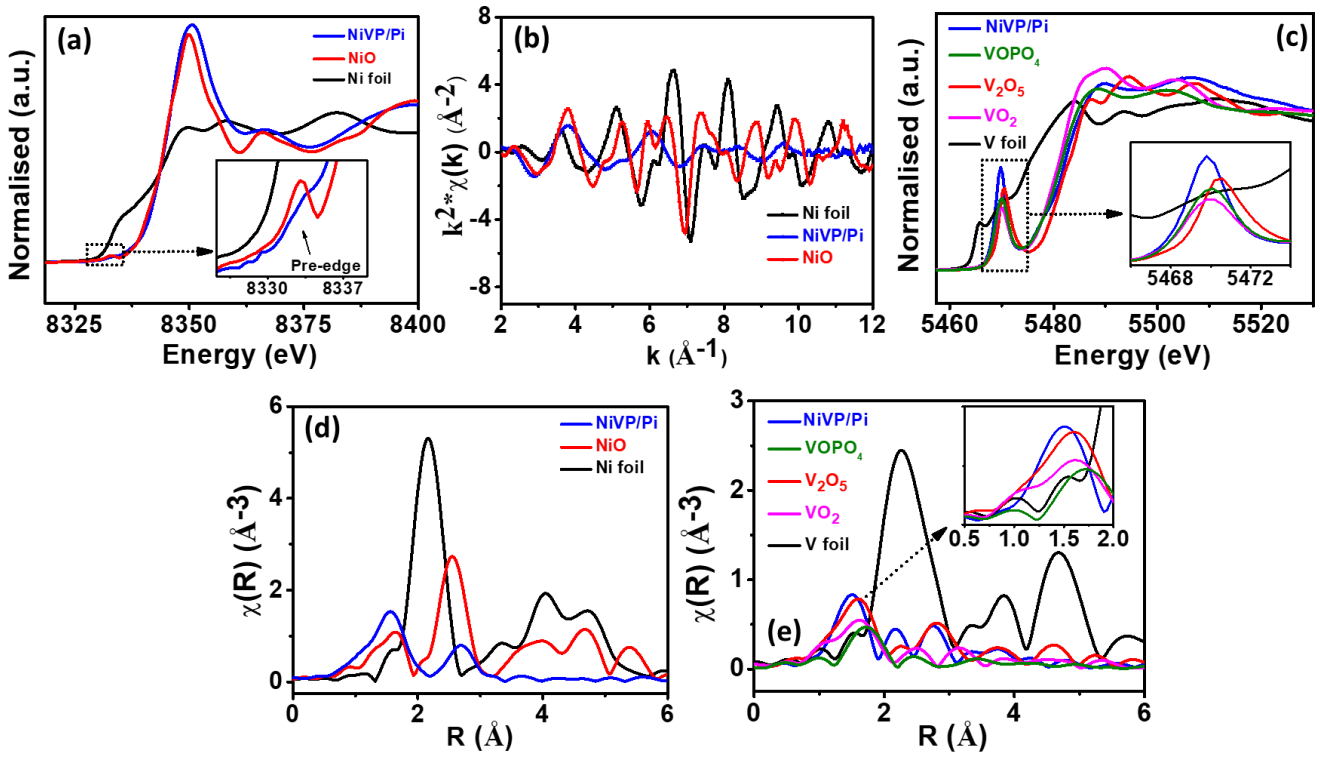

Fig. 2 XANES and EXAFS spectra. (a) Normalised XANES spectra of NiVP/Pi along with standard samples at Ni K-edge, (b) EXAFS oscillation of NiVP/Pi along with standard samples in k-space at Ni K-edge, (c) XANES spectra of NiVP/Pi and Fourier transformed EXAFS spectrum at (d) Ni K-edge and (e) V K-edge of NiVP/Pi along with standards.

The electrochemical performance of the proposed S@NiVP/Pi-NCS anode was initially evaluated by cyclic voltammetry (CV) measurements in Ar saturated 2 M aqueous Na_2SO_4 electrolyte over a potential range of 0.4 V to -1.0 V at a scan rate of 2 mV s^{-1} in a three-electrode assembly using stainless steel (SS 316) and Ag/AgCl/3M KCl as counter and reference electrode respectively. The obtained CV (Fig. 3a) shows a well-defined redox behaviour exhibiting two clear cathodic and anodic peaks corresponding to sulfur reduction-oxidation reaction. The initial reduction peak *ca.* -

0.64 V attributed to sodiation of S_8 to higher-order polysulfide followed by second reduction peak *ca.* -0.76 V ascribed to a subsequent reduction of higher polysulfide to final discharge product Na_2S_2/Na_2S or HS^{-1}. On the other hand one oxidation peaks *ca.* -0.3 V and a feeble peak at *ca.* -0.1 V was observed which can be attributed to the conversion of HS^{-1}/Na_2S to Na_2S_4 and Na_2S_4 to S_8 signifying the reversibility of the process.[35] Interestingly, S@NiVP/Pi-NCS shows high reversibility without any significant changes either in peak potential or peak current even after 50 cycles validating faster redox kinetics and efficient polysulfide anchoring (Fig. 3b and Supplementary Fig. 7). In order to understand the anchoring ability and the polysulfide conversion of the proposed anode, control experiments were performed using S@NiVP/Pi, which exhibits only one reduction peak *ca.* -0.67 V and two oxidation peaks *ca.* -0.37 V and *ca.* -0.19 V wherein the second oxidation peak is more pronounced in S@NiVP/Pi suggesting an enhanced redox kinetics of the polysulfide conversion by NiVP/Pi (Fig. 3c). The comparative CV of both S@NiVP/Pi-NCS and S@NiVP/Pi (Supplementary Fig. 8a) reveals that both oxidation and reduction peak current are two times higher for S@NiVP/Pi-NCS.

Notably, the obtained behaviour is different from most of the previously reported aqueous sulfur-based batteries in which normally single anodic peak was observed due to sluggish kinetics to catalyse the rapid conversion of insulating Na_2S to S_8.[36] Thus, the observed second oxidation peak endorses that S@NiVP/Pi-NCS not only have suitable anchoring sites to inhibit the polysulfide dissolution but also enhance redox kinetics of the adsorbed polysulfide by facile transport of electrons. The accelerated redox kinetics by S@NiVP/Pi-NCS was further elucidated by electrochemical impedance spectroscopic (EIS) measurements. The EIS spectra depicted in Fig. 3d reveals lower solution (R_s) and charge transfer resistance (R_{ct}) for S@NiVP/Pi-NCS than S@NiVP/Pi reinforces the fact that S@NiVP/Pi-NCS exhibit faster kinetics at the electrode-electrolyte interface. Moreover, angle of the Warburg region for S@NiVP/Pi-NCS is higher than S@NiVP/Pi signifying that process is not completely under diffusion control but has some

capacitive nature due to the larger surface area and conductive nature of NCS.[25] Further, to ascertain the kinetics of electron transfer at the electrode-electrolyte interface exchange current density and rate constant were calculated from EIS spectra using the following equations.[37,38]

$R_{ct} = RT/nFi_0$ ---------- (1)

$R_{ct} = RT/n^2F^2Ack^0$----------(2)

Where R is gas constant, T is temperature, n is no. of electron transfer, F is the Faraday constant, R_{ct} is charge transfer resistance, i_o is exchange current density, and k^0 is the rate constant. The exchange current density as well as the rate constant for S@NiVP/Pi-NCS was found to be higher (1.62×10^{-3} mA cm^2, 2.84×10^{-6} cm s^{-1} respectively) compared to S@NiVP/Pi (1.18×10^{-3} mA cm^2, 2.05×10^{-6} cm s^{-1} respectively) demonstrating the accelerated rate of the reaction. This was further complemented from the Tafel slope extracted from CV (Supplementary Figs. 8b & 8c) wherein S@NiVP/Pi-NCS exhibits a lower Tafel slope of 30 mV dec^{-1} compared to S@NiVP/Pi (57 mV dec^{-1}). These observations were equally supported by the higher diffusion coefficient for S@NiVP/Pi-NCS (3.5×10^{-9} cm^2 s^{-1}) compared to S@NiVP/Pi (1.9×10^{-9} cm^2 s^{-1}), indicating a faster Na^+ diffusion and interconversion of sulfur to polysulfide and *vice versa* (detailed in supplementary information). These results are well complimented by lower activation energy for polysulfide conversion (Supplementary Figs. 9-13)

Further, CVs at different scan rates for S@NiVP/Pi-NCS (Fig. 3e) shows negligible changes in peak potential with increase in scan rate demonstrating the faster kinetics and high reversibility. More importantly, the second feeble oxidation peak can be seen clearly even at all the scan rates demonstrating the superior activity of NiVP/Pi-NCS catalyst to catalyse the polysulfide redox kinetics even at elevated scan rate. To comprehend the proposed anode for battery applications, galvanostatic charge-discharge experiments were performed using a similar three-electrode system. The charge-discharge profile at 0.5 C in Fig. 3f displaying two clear discharge plateaus at *ca.* -0.62 V and -0.75 V, respectively. The voltage plateau at *ca*. -0.62 V ascribed to the reduction of

elemental sulfur (S_8) to higher-order polysulfide (Na_2S_x, $4<x<8$). Further, sweeping potential to more cathodic region, the second plateau at *ca.* -0.75 V was appeared due to the reduction of higher-order polysulfide to lower-order polysulfide (Na_2S_x,$4>n$) and finally to Na_2S/HS^{-1}. As depicted in Figs. 3f & 3g, S@NiVP/Pi-NCS shows an excellent performance with a very high specific capacity of 826 mA h g^{-1} at 0.5 C [based on S loading, which is 77 % of theoretical S capacity (1072 mA h g^{-1}) detailed in Supplementary] with an average loading of 1.426 mg cm^{-2} w.r.t. sulfur. While S@NiVP/Pi shows 667 mA h g^{-1} of capacity at 0.5 C under similar conditions (Supplementary Figs. 14 and 15). The obtained capacity is very high compared to the previously reported literature for ARSIBs (Supplementary Table 5). Notably, NiVP/Pi and NiVP/Pi-NCS contributed only 30 mA h g^{-1} and 45 mA h g^{-1} due to pseudocapacitive Na^+ storage, which demonstrating that sulfur is contributing towards maximum capacity (Supplementary Fig. 16 & 17).

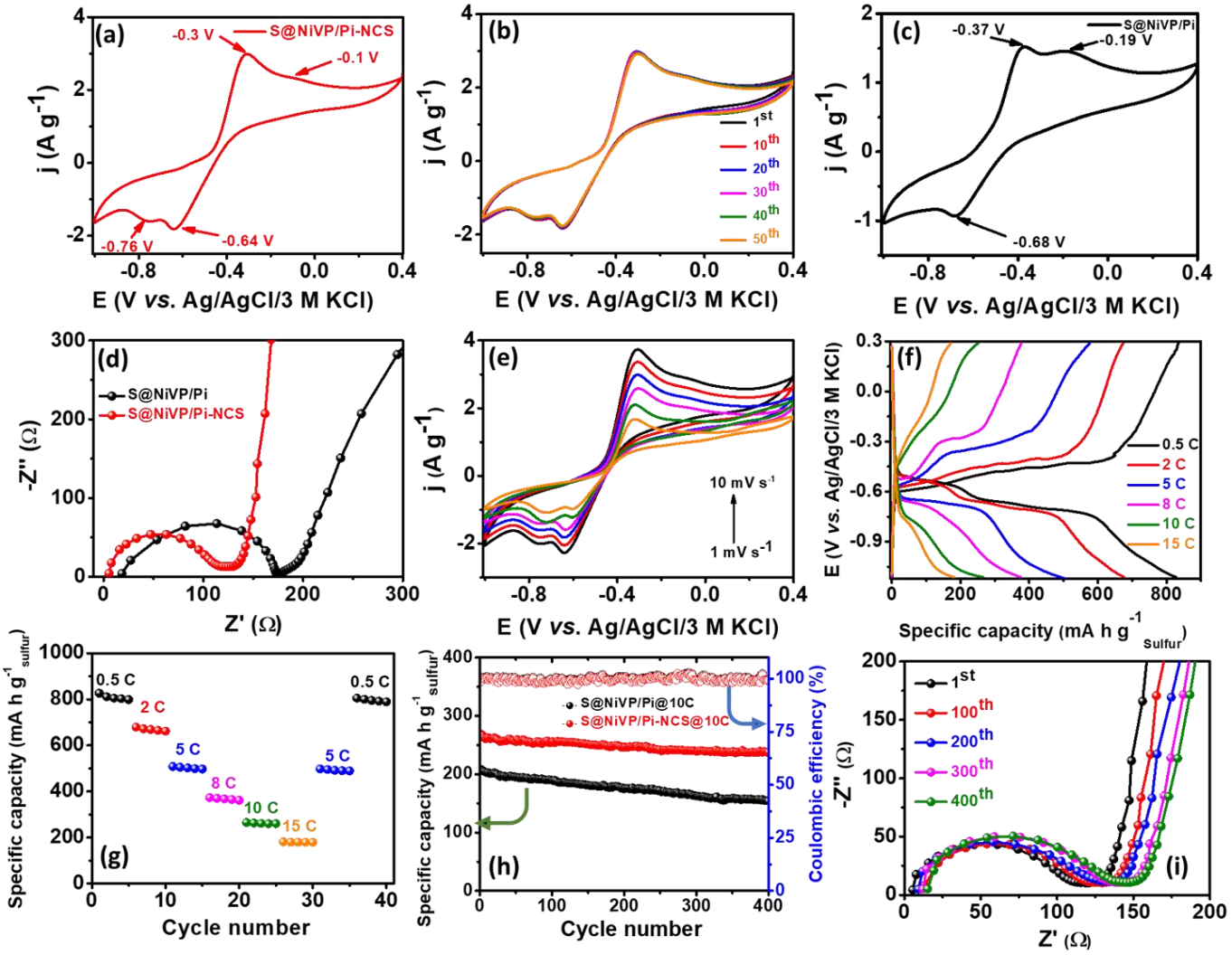

Fig. 3. Electrochemical and battery performance. (a) Cyclic voltammogram, (b) cyclic stability of S@NiVP/Pi-NCS for 50 cycles at 2 mV s^{-1} and (c) CV of S@NiVP/Pi anode at 2 mV s^{-1} (d) EIS spectra of respective anode, (e) CVs at various scan rates (f) voltage profile of S@NiVP/Pi-NCS, (g) rate performance of S@NiVP/Pi-NCS at different C-rates, (h) long term cycling performance of various anodes at 10 C over 400 cycles in 2M aq. Na_2SO_4 and (i) corresponding EIS during cycling performance.

To comprehend the synergy between the anchoring strength towards polysulfide and it's catalytic conversion by S@NiVP/Pi-NCS, charge-discharge experiments were performed at various C-rates from 0.5 C to 15 C. As observed from Fig. 3g the S@NiVP/Pi-NCS displays superior

specific capacity at all C-rates and both charge-discharge capacities remain stable at various C-rates. When C-rate was increased to 2 C, the specific capacity was 679 mA h g^{-1}, followed by 373 mA h g^{-1} at 8 C. It is noteworthy to mention that S@NiVP/Pi-NCS maintains 265 mA h g^{-1} and 181 mA h g^{-1} capacity even at a very high C-rate of 10 C and 15 C which further retains its original capacity of 805 mA h g^{-1} when switched back to 0.5 C demonstrating an outstanding rate performance by S@NiVP/Pi-NCS which are superior compared to S@NiVP/Pi (Supplementary Fig. 14a & 15b). More importantly, 89 % of capacity retention was observed for S@NiVP/Pi-NCS even after 400 cycles (Fig. 3h) at a very high C-rate of 10 C while S@NiVP/Pi exhibits 74 % retention with a capacity decay of 0.065 % per cycle (Supplementary Fig. 14c & 15c). These results demonstrating that S@NiVP/Pi-NCS is a promising anode with almost 100 % of columbic efficiency with a negligible capacity decay of 0.03 % per cycle (Fig. 3h) which corresponds to the high utilization of sulfur, which is an achievement against the prime obstacles in aqueous rechargeable sulfur batteries. Further, the battery cell was monitored by EIS studies during cycling process to keep track of resistance at electrode-electrolyte interface. As observed in Fig. 3i, both R_s and R_{ct} increase by a small magnitude for S@NiVP/Pi-NCS compared to S@NiVP/Pi (Supplementary Fig. 14d), demonstrating its the superior rate performance of S@NiVP-NCS.

Control experiments with S@NiP/Pi shows only one redox peak in CV and the charge-discharge profile displays an initial capacity of 609.2 mA h g^{-1} (w.r.t. sulfur loading) at 0.5 C which reduced to 74.16 mA h g^{-1} at 15 C (Supplementary Fig. 18). Stability studies at 10 C demonstrate only 53 % capacity retention with a capacity loss of 0.12 % per cycle. These results demonstrating the importance of vanadium in the NiVP/Pi catalyst for entrapment and conversion of sodium polysulfides. As suggested from XANES, high oxidation state V (+4 and +5; most likely in the form of $VOPO_4$) and higher degree of distortion due to orbital overlap in NiVP/Pi activated the vanadium center highly susceptible for nucleophilic attack of polysulfide and enhances the kinetics of the polysulfide conversion. These observations are well supported by the shift in the binding

energy of V 2p after discharge (detailed later in XPS). Due to strong chemical interaction and polysulfide adsorption, the cycling stability was improved significantly in NiVP/Pi than NiP/Pi.

The polysulfide anchoring ability by various catalyst was further analysed by visualization and UV-vis studies, wherein 10 mg of various catalysts were added to 3 mL of deaerated 3 mM Na_2S solution in sealed vials and sonicated for 10 minutes. As observed from Fig. 4a (Supplementary Fig. 19) as prepared Na_2S solution shows yellow colour which disappeared after the addition of NiVP/Pi-NCS (after 30 min) and a similar observation was noted in the case of NiVP/Pi catalyst as well. Whereas, NCS-alone shows a slight yellowish solution and was further supported by UV-vis studies (Fig. 4b). In addition, to get more insight into the nature of the product during the cycling process, the electrolyte was monitored by *in situ* UV-Vis Spectro-electrochemical studies (Fig. 4c-d, & Supplementary Fig. 20). The UV-spectra in Fig. 4d & Supplementary Fig. 21-22 shows a feeble broad peaks around 300 nm, 370 nm, and 420 nm corresponds to short-chain polysulfide (S_2^{2-} - S_4^{2-}).[39] Interestingly the relative increase in peak intensity was observed after 400 cycles, although no noticeable colour change of the electrolyte was observed (Fig. 4c). In comparison, the S@NiVP/Pi shows relatively high absorbance compared to S@NiVP/Pi-NCS. The quantitative estimation of sulfur lost by UV-Vis studies (detailed in Supplementary Fig. 22 & Supplementary Table 3) was found to be 8.65 % and 23 % for S@NiVP/Pi-NCS and S@NiVP/Pi respectively after 400 cycles, which is well complemented by potentiometric titration analysis (Supplementary Fig. 23 & Supplementary Table 4 & 5). From these observations it is evident that a negligible amount of sulfur is lost even after prolonged 400 cycling thus signifies that NiVP/Pi-NCS together play a substantial role in facile adsorption and conversion of polysulfides to sulfur and *vice versa*.

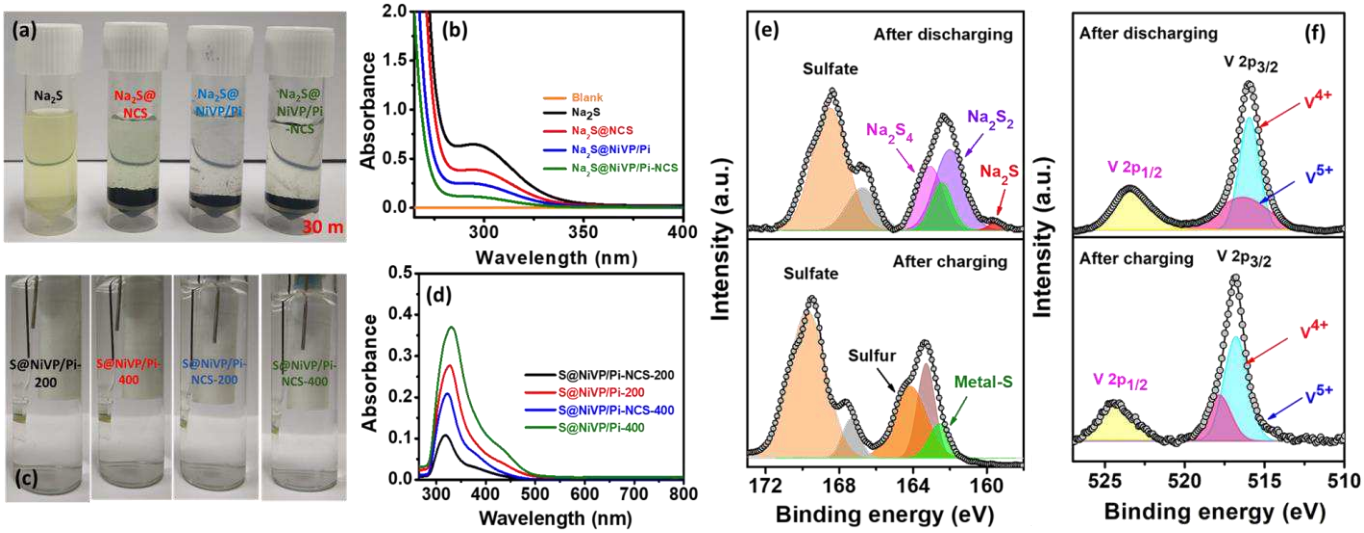

Fig. 4. Visual observation, UV and XPS analysis of S@NiVP/Pi-NCS after charge-discharge process

(a) Photographic images of Na_2S solution with various catalyst after 30 minutes, (b) corresponding UV-vis spectra of Na_2S solution of fig. 4a after 30 minutes (c) photographic images of 2 M aq. Na_2SO_4 electrolyte with S@NiVP/Pi-NCS and S@NiVP/Pi anodes after 200 and 400 cycles, and (d) corresponding UV-vis spectra of dissolved polysulfide in 2 M aq. Na_2SO_4 at various cycling performance, deconvoluted XP spectra of (e) S 2p, and (f) V 2p of S@NiVP/Pi-NCS anode after charge and discharge cycles.

To illustrate the chemical interaction between NiVP/Pi and polysulfide after charge-discharge process, in-depth post analysis by XPS was carried out by retrieving the sample after 400 charge-discharge cycles followed by thorough washing with deionized water. The XP survey spectra of S@NiVP/Pi-NCS reveals the presence of all the elements Ni, V, P, O, C and N after both the charge and discharge process (Supplementary Fig. 24 & 25). After discharge process, the deconvoluted XP spectra of S 2p (Fig. 4e) display peaks at 161.9 eV and 163.0 eV corresponds to the formation of lower order polysulfides Na_2S_2 and Na_2S_4 along with a peak at 159.8 eV corresponds to Na_2S.[36,40] On the other hand, on charging the peak due to polysulfide disappeared and a new peak at 164.3 eV was observed corresponding to elemental sulfur.[27] More importantly, another peak observed at 162.5 eV for both charging and discharging process attributed to the formation of metal-sulfides,

confirming the interaction of polysulfide with NiVP/Pi. In addition, a high-intense peak at 168-170 eV during charge and discharge show the presence of sulfate from electrolyte. Further, the formation of intermediate polysulfide were analysed by XP S 2p spectra at various discharge potentials (detailed in Supplementary Fig. S26). Further, deconvoluted Ni 2p XP spectra show a minimal change in the binding energy before and after the charging. Interestingly after discharging the V $2p_{3/2}$ and V $2p_{1/2}$ shifted towards lower binding energy compared to pristine NiVP/Pi suggesting enhanced electron density on vanadium (Fig. 4f). Meanwhile, after charging, the peaks shifted to their original position. The shift in the binding energy during discharging possibly due to the chemical bonding of polysulfide with vanadium.

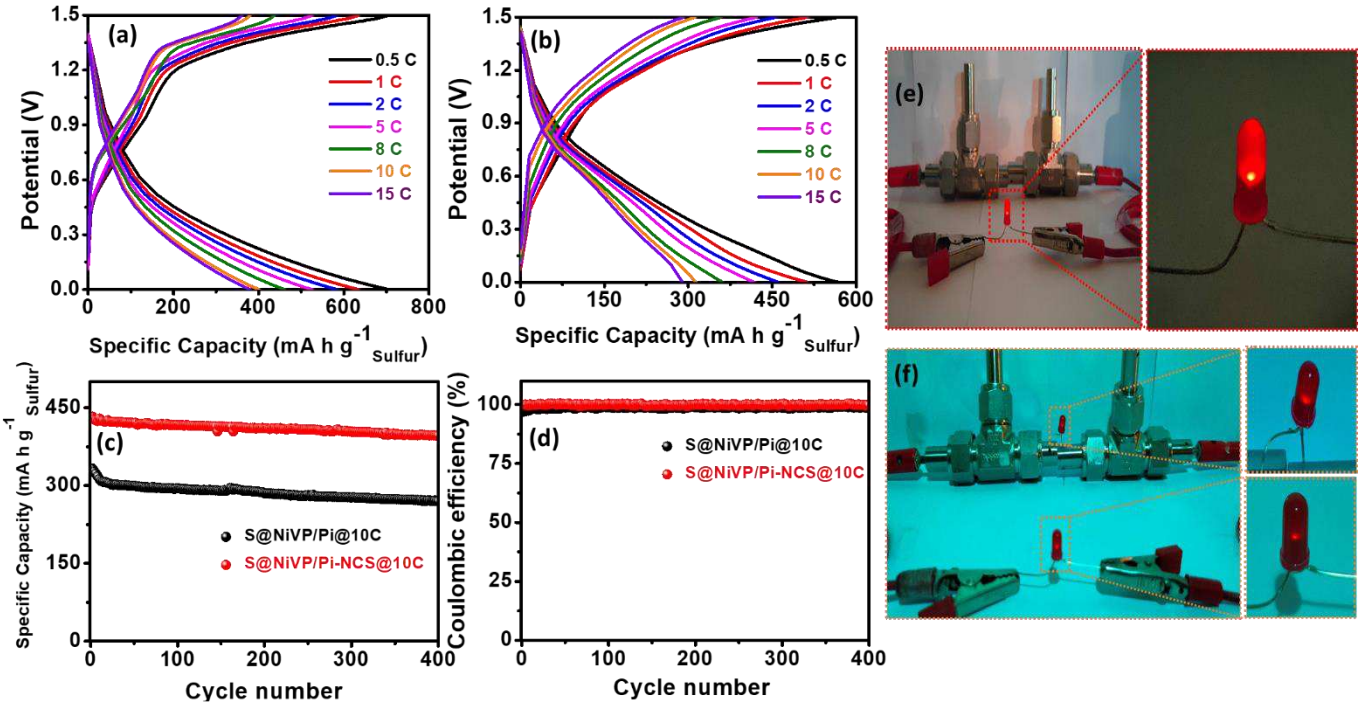

Fig. 5: Full cell battery performance. Galvanostatic charge-discharge curves of full cell battery assembled using (a) S@NiVP/Pi-NCS anode + $Na_{0.44}MnO_2$ cathode and (b) S@NiVP/Pi anode + $Na_{0.44}MnO_2$ cathode at various C-rates, (c and d) corresponding battery cycling performance and coulombic efficiency at 10 C respectively over 400 cycles in 2 M aq. Na_2SO_4, (e), and (f) demonstration of two aqueous Na-ion/S battery consisting of S@NiVP/Pi-NCS anode and $Na_{0.44}MnO_2$ cathode powering LED.

Further, full cell battery performance was analysed by assembling a battery using Swagelok - cell with two-electrode setup having proposed S@NiVP/Pi-NCS anode and a $Na_{0.44}MnO_2$ cathode in 2 M Na_2SO_4 electrolyte. The loading of cathode to anode was fixed at 4.14:1, and the full cell analysis was performed in the potential range of 0 V to 1.5 V. The galvanostatic charge-discharge analysis at 0.5 C (Fig. 5a and Supplementary Fig. 28 & 29) displays a very high initial specific capacity of 705 mA h g^{-1} w.r.t the weight of sulfur and 91.71 mA h g^{-1} capacity w.r.t total electrode weight respectively. On the other hand, the S@NiVP/Pi anode and $Na_{0.44}MnO_2$ cathode (Fig. 5b and Supplementary Fig. 29) battery cell delivers an initial capacity of 567 mA h g^{-1} w.r.t the weight of sulfur and 84.25 mA h g^{-1} w.r.t total electrode weight, respectively. Further, the rate performance of the full cell was analyzed by subjecting it to various C-rates. Interestingly, both the full cell (S@NiVP/Pi-NCS and S@NiVP/Pi anodes with $Na_{0.44}MnO_2$ cathode) can successfully operate at high C rates and achieved 380 mA h g^{-1} and 290 mA h g^{-1} of capacity even at a very high C-rate of 15 C, demonstrating the ability of the catalyst to operate under uphill C-rates (Fig. 5a & 5b and Supplementary Fig. 28 and 29). Further, the proposed S@NiVP/Pi-NCS is a promising anode exhibiting an exceptionally high-rate performance witnessed from 100 % CE (Fig. 5d) and could able to retain 91 % of its initial capacity even after 400 prolonged cycling at a very high C-rate of 10 C compared to S@NiVP/Pi (81 %) (Fig. 5c, Supplementary Fig. 30). Besides, from developing a cost-effective and safer energy storage system towards practical application, we have demonstrated a device based on two aqueous Na –ion/S full cell after a full charge and connected in series. Fig. 5e & 5f and movie S1 show an optical image of the device powering a glowing red LED. Further, the assembled device can simultaneously lighten two LEDs, demonstrating the practical applicability of such types of devices.

Conclusions

In summary, we have demonstrated novel high-capacity aqueous Na-ion/S batteries with S@NiVP/Pi-NCS anode using 70 % of elemental sulfur. Synthesized catalyst combines the merits of high conductivity and entrapment ability of NCS with high anchoring and polysulfide redox kinetic ability of

polar NiVP/Pi to accomplish smooth diffusion-immobilization and accelerated conversion of polysulfide. The high intrinsic catalytic activity of NiVP/Pi-NCS is mainly due to high conductivity, facile electron transfer, high polysulfide conversion kinetics and good anchoring of polysulfides even in aqueous media. Various electrochemical, spectroscopic and visualization studies confirmed that the anode could inhibit the polysulfide dissolution in aqueous electrolyte due to its favourable anchoring sites. Moreover, the accelerated redox kinetics towards the polysulfide conversion at the S@NiVP/Pi-NCS anode enables the catalyst to operate at a very high current density of 10 C. The S@NiVP/Pi-NCS anode delivers an outstanding capacity of 826 mA h g^{-1} at 0.5 C with an excellent cycling performance over 400 cycles at a very high current density of 10 C. Further, the full cell was assembled by using S@NiVP/Pi-NCS anode, and $Na_{0.44}MnO_2$ cathode which demonstrates the excellent initial capacity of 705 mA h g^{-1} at 0.5 C and shows 91 % of capacity retention after 400 cycles at 10 C and two fully charged cell connected in series able to power two LED demonstrate its practical application. We believe that the present work paves the way for designing a low cost and highly stable anode for aqueous sodium ion battery technology for large storage applications.

Conflicts of interest

There are no conflicts to declare.

References:

1 Su, Y.-S., Fu, Y., Cochell, T. & Manthiram, A. A strategic approach to recharging lithium-sulphur batteries for long cycle life. *Nat. Commun.* **4**, 1-8 (2013).

2 Ansari, Y., Zhang, S., Wen, B., Fan, F. & Chiang, Y. M. Stabilizing Li–S Battery Through Multilayer Encapsulation of Sulfur. *Adv. Energy Mater.* **9**, 1802213 (2019).

3 Deng, N. *et al.* Functional mechanism analysis and customized structure design of interlayers for high performance Li-S battery. *Energy Storage Mater.* **23**, 314-349 (2019).

4 Liu, M. *et al.* A Review: Electrospun Nanofiber Materials for Lithium-Sulfur Batteries. *Adv. Funct. Mater.* **29**, 1905467 (2019).

5 Perveen, T. *et al.* Prospects in anode materials for sodium ion batteries-A review. *Renew. Sustain. Energy. Rev.* **119**, 109549 (2020).

6 Shao, T. *et al.* Electrolyte regulation enhances the stability of Prussian blue analogues in aqueous Na-ion storage. *J. Mater. Chem. A* **7**, 1749-1755 (2019).

7 Tron, A., Jo, Y. N., Oh, S. H., Park, Y. D. & Mun, J. Surface modification of the LiFePO4 cathode for the aqueous rechargeable lithium ion battery. *ACS Appl. Mater. Interfaces* **9**, 12391-12399 (2017).

8 Li, Z., Young, D., Xiang, K., Carter, W. C. & Chiang, Y. M. Towards high power high energy aqueous sodium-ion batteries: the $NaTi_2(PO_4)_3/Na_{0.44}MnO_2$ system. *Adv. Energy Mater.* **3**, 290-294 (2013).

9 Chao, D. *et al.* Roadmap for advanced aqueous batteries: From design of materials to applications. *Sci. Adv.* **6**, eaba4098 (2020).

10 Suo, L. *et al.* "Water-in-salt" electrolyte enables high-voltage aqueous lithium-ion chemistries. *Science* **350**, 938-943 (2015).

11 Jiang, L. *et al.* High-Voltage Aqueous Na-Ion Battery Enabled by Inert-Cation-Assisted Water-in-Salt Electrolyte. *Adv. Mater.* **32**, 1904427 (2020).

12 Nakamoto, K., Kano, Y., Kitajou, A. & Okada, S. Electrolyte dependence of the performance of a $Na_2FeP_2O_7//NaTi_2(PO_4)_3$ rechargeable aqueous sodium-ion battery. *J. Power Sources* **327**, 327-332 (2016).

13 Lei, P., Liu, K., Wan, X., Luo, D. & Xiang, X. Ultrafast Na intercalation chemistry of $Na_2Ti_{3/2}Mn_{1/2}(PO_4)_3$ nanodots planted in a carbon matrix as a low cost anode for aqueous sodium-ion batteries. *Chem. Commun.* **55**, 509-512 (2019).

14 Zhang, F., Li, W., Xiang, X. & Sun, M. Highly stable Na-storage performance of $Na_{0.5}Mn_{0.5}Ti_{0.5}O_2$ microrods as cathode for aqueous sodium-ion batteries. *J. Electroanal. Chem.* **802**, 22-26 (2017).

15 Zhang, X. *et al.* Na-birnessite with high capacity and long cycle life for rechargeable aqueous sodium-ion battery cathode electrodes. *J. Mater. Chem. A* **4**, 856-860 (2016).

16 Fonsaca, J. E., Domingues, S. H., Orth, E. S. & Zarbin, A. J. A black phosphorus-based cathode for aqueous Na-ion batteries operating under ambient conditions. *Chem. Commun.* (2020).

17 Wang, J. *et al.* Sodium-rich iron hexacyanoferrate with nickel doping as a high performance cathode for aqueous sodium ion batteries. *J. Electroanal. Chem.* **818**, 10-18 (2018).

18 Jiang, P. *et al.* Polyethylene Glycol–Na+ Interface of Vanadium Hexacyanoferrate Cathode for Highly Stable Rechargeable Aqueous Sodium-Ion Battery. *ACS Appl. Mater. Interfaces* **11**, 28762-28768 (2019).

19 Yuan, Y. *et al.* Intercalation Pseudocapacitive Nanoscale Nickel Hexacyanoferrate@Carbon Nanotubes as a High-Rate Cathode Material for Aqueous Sodium-Ion Battery. *ACS Sustain. Chem. Eng.* (2020).

20 Baster, D., Oveisi, E., Mettraux, P., Agrawal, S. & Girault, H. H. Sodium chromium hexacyanoferrate as a potential cathode material for aqueous sodium-ion batteries. *Chem. Commun.* **55**, 14633-14636 (2019).

21 Ke, L. *et al.* A $NaV_3(PO_4)_3$@C hierarchical nanofiber in high alignment: exploring a novel high-performance anode for aqueous rechargeable sodium batteries. *Nanoscale* **9**, 4183-4190 (2017).

22 Qiu, S. *et al.* NASICON-type $Na_3Fe_2(PO_4)_3$ as a low-cost and high-rate anode material for aqueous sodium-ion batteries. *Nano Energy* **64**, 103941 (2019).

23 Wu, F. *et al.* Layered $LiTiO_2$ for the protection of Li_2S cathodes against dissolution: mechanisms of the remarkable performance boost. *Energy Environ. Sci.* **11**, 807-817 (2018).

24 Zhou, T. *et al.* Twinborn TiO_2–TiN heterostructures enabling smooth trapping–diffusion–conversion of polysulfides towards ultralong life lithium–sulfur batteries. *Energy Environ. Sci.* **10**, 1694-1703 (2017).

25 Wu, X. *et al.* A high-capacity dual core–shell structured MWCNTs@ S@PPy nanocomposite anode for advanced aqueous rechargeable lithium batteries. *Nanoscale* **9**, 11004-11011 (2017).

26 Shao, J., Li, X., Zhang, L., Qu, Q. & Zheng, H. Core–shell sulfur@ polypyrrole composites as high-capacity materials for aqueous rechargeable batteries. *Nanoscale* **5**, 1460-1464 (2013).

27 Yang, C. *et al.* Unique aqueous Li-ion/sulfur chemistry with high energy density and reversibility. *Proc. Natl. Acad. Sci.* **114**, 6197-6202 (2017).

28 Tekin, B., Sevinc, S., Morcrette, M. & Demir-Cakan, R. A New Sodium-Based Aqueous Rechargeable Battery System: The Special Case of Na0. 44MnO2/Dissolved Sodium Polysulfide. *Energy Technol.* **5**, 2182-2188 (2017).

29 Tiwari, A., Singh, V., Mandal, D. & Nagaiah, T. C. Nitrogen containing carbon spheres as an efficient electrocatalyst for oxygen reduction: Microelectrochemical investigation and visualization. *J. Mater. Chem. A* **5**, 20014-20023 (2017).

30 Fan, K. *et al.* Nickel–vanadium monolayer double hydroxide for efficient electrochemical water oxidation. *Nat. Commun.* **7**, 1-9 (2016).

31 Park, H. W., Chae, J. S., Park, S.-M., Kim, K.-B. & Roh, K. C. Nickel-based layered double hydroxide from guest vanadium oxide anions. *Met. Mater. Int.* **19**, 887-894 (2013).

32 Song, Y. *et al.* Synchronous immobilization and conversion of polysulfides on a VO_2–VN binary host targeting high sulfur load Li–S batteries. *Energy Environ. Sci.* **11**, 2620-2630 (2018).
33 Wang, D. *et al.* Atomic and electronic modulation of self-supported nickel-vanadium layered double hydroxide to accelerate water splitting kinetics. *Nat. Commun.* **10**, 1-12 (2019).
34 Liu, P. F. *et al.* $Ni_2P(O)/Fe_2P(O)$ interface can boost oxygen evolution electrocatalysis. *ACS Energy Lett.* **2**, 2257-2263 (2017).
35 Wang, N. *et al.* High-performance room-temperature sodium-sulfur battery enabled by electrocatalytic sodium polysulfides full conversion. *Energy Environ. Sci.* (2020).
36 Wei, S. *et al.* A stable room-temperature sodium–sulfur battery. *Nat. Commun.* **7**, 11722 (2016).
37 Swamy, T. & Chiang, Y.-M. Electrochemical charge transfer reaction kinetics at the silicon-liquid electrolyte interface. *J. Electrochem. Soc.* **162**, A7129-A7134 (2015).
38 Randviir, E. P. A cross examination of electron transfer rate constants for carbon screen-printed electrodes using Electrochemical Impedance Spectroscopy and cyclic voltammetry. *Electrochim. Acta* **286**, 179-186 (2018).
39 Zhang, M. *et al.* Highly efficient H_2 production from H_2S via a robust graphene-encapsulated metal catalyst. *Energy Environ. Sci.* **13**, 119-126 (2020).
40 Fantauzzi, M., Elsener, B., Atzei, D., Rigoldi, A. & Rossi, A. Exploiting XPS for the identification of sulfides and polysulfides. *RSC Adv.* **5**, 75953-75963 (2015).

Figures

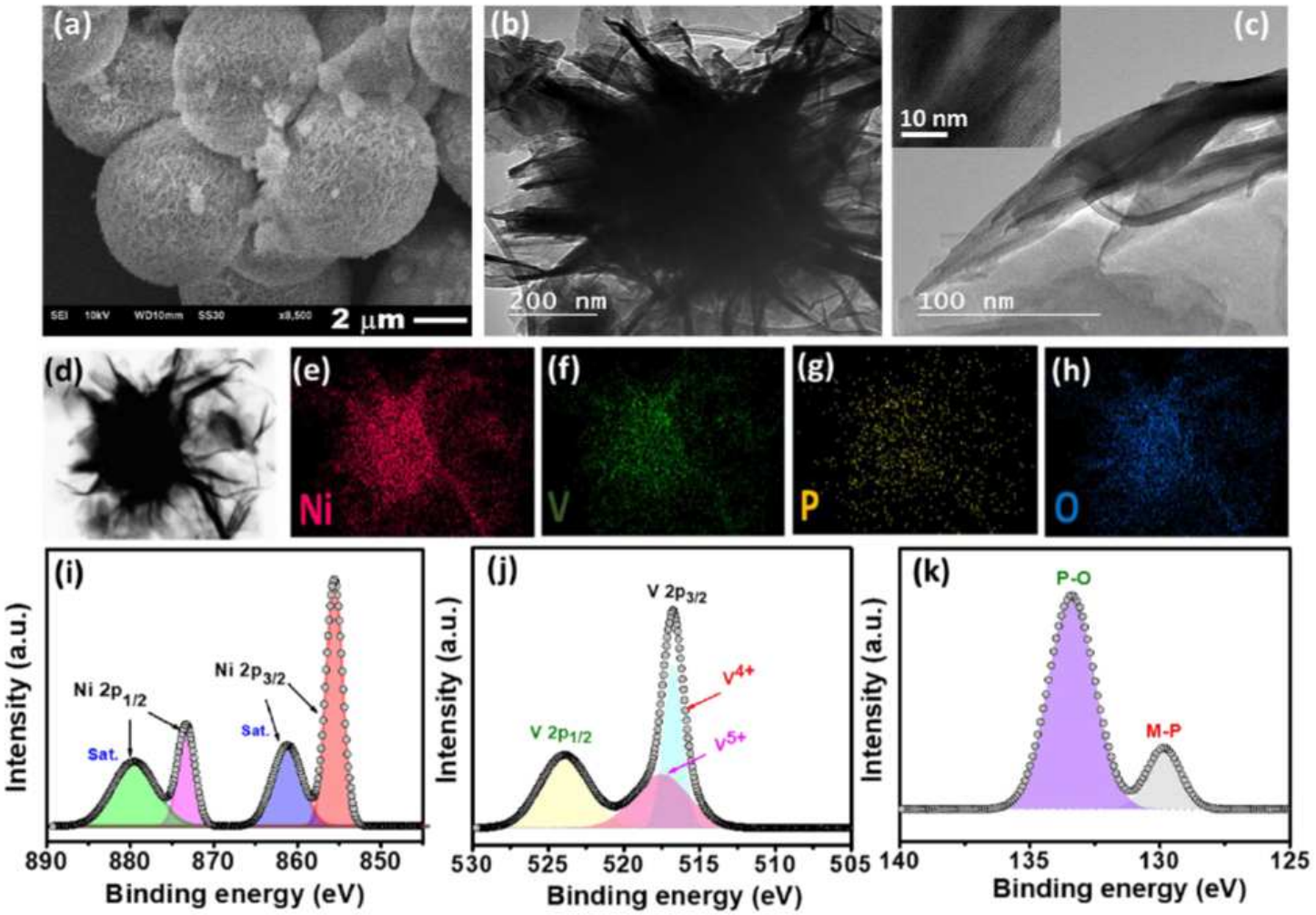

Figure 1

Microstructure, morphology characteristics and XPS of NiVP/Pi. (a) SEM, (b) TEM and (c) HTEM images of NiVP/Pi, (d) STEM image of NiVP/Pi and corresponding EDS elemental dot mapping images of (e) nickel, (f) vanadium, (g) phosphorous and (h) oxygen, deconvoluted XP spectra of (i) Ni 2p, (j) V 2p, and (k) P 2p of NiVP/Pi.

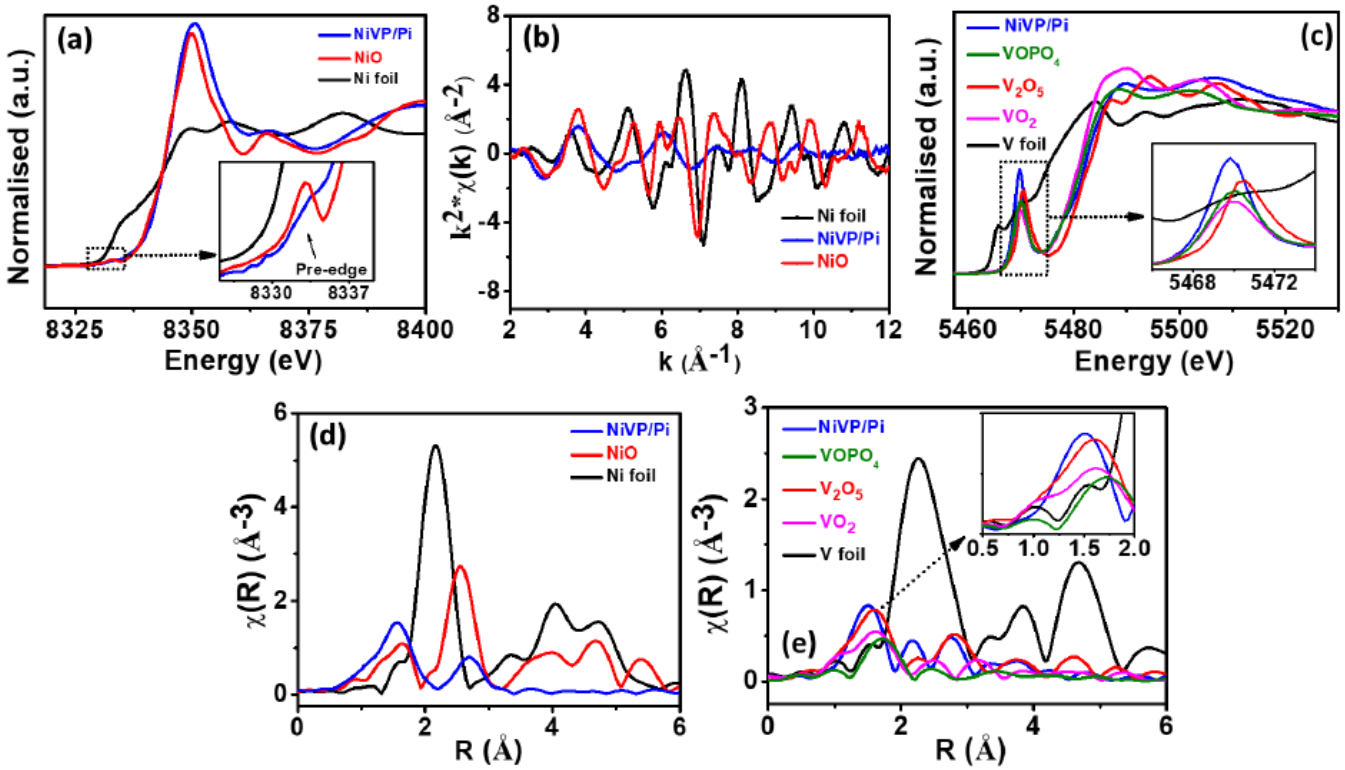

Figure 2

XANES and EXAFS spectra. (a) Normalised XANES spectra of NiVP/Pi along with standard samples at Ni K-edge, (b) EXAFS oscillation of NiVP/Pi along with standard samples in k-space at Ni K-edge, (c) XANES spectra of NiVP/Pi and Fourier transformed EXAFS spectrum at (d) Ni K-edge and (e) V K-edge of NiVP/Pi along with standards.

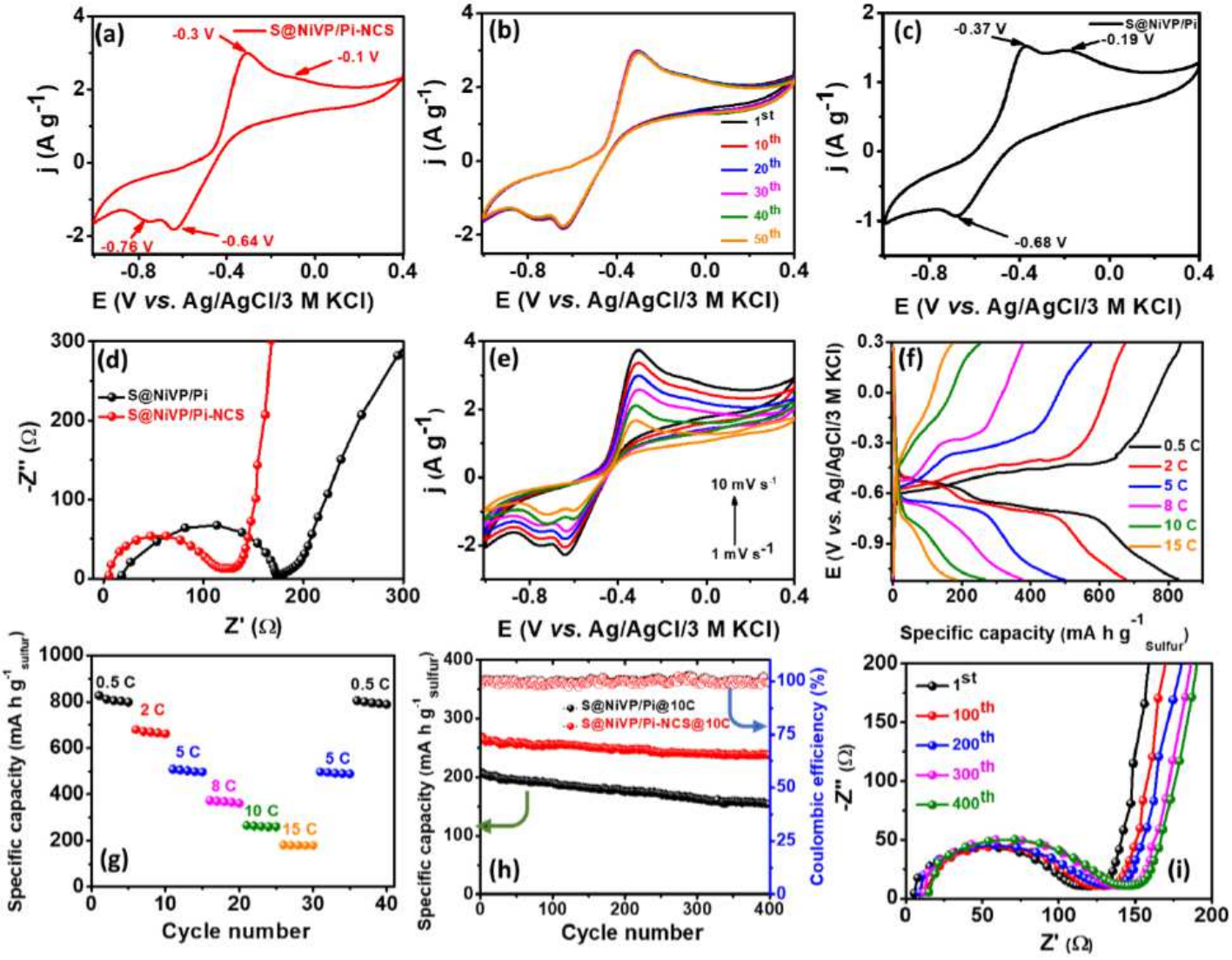

Figure 3

Electrochemical and battery performance. (a) Cyclic voltammogram, (b) cyclic stability of S@NiVP/Pi-NCS for 50 cycles at 2 mV s-1 and (c) CV of S@NiVP/Pi anode at 2 mV s-1 (d) EIS spectra of respective anode, (e) CVs at various scan rates (f) voltage profile of S@NiVP/Pi-NCS, (g) rate performance of S@NiVP/Pi-NCS at different C-rates, (h) long term cycling performance of various anodes at 10 C over 400 cycles in 2M aq. Na2SO4 and (i) corresponding EIS during cycling performance.

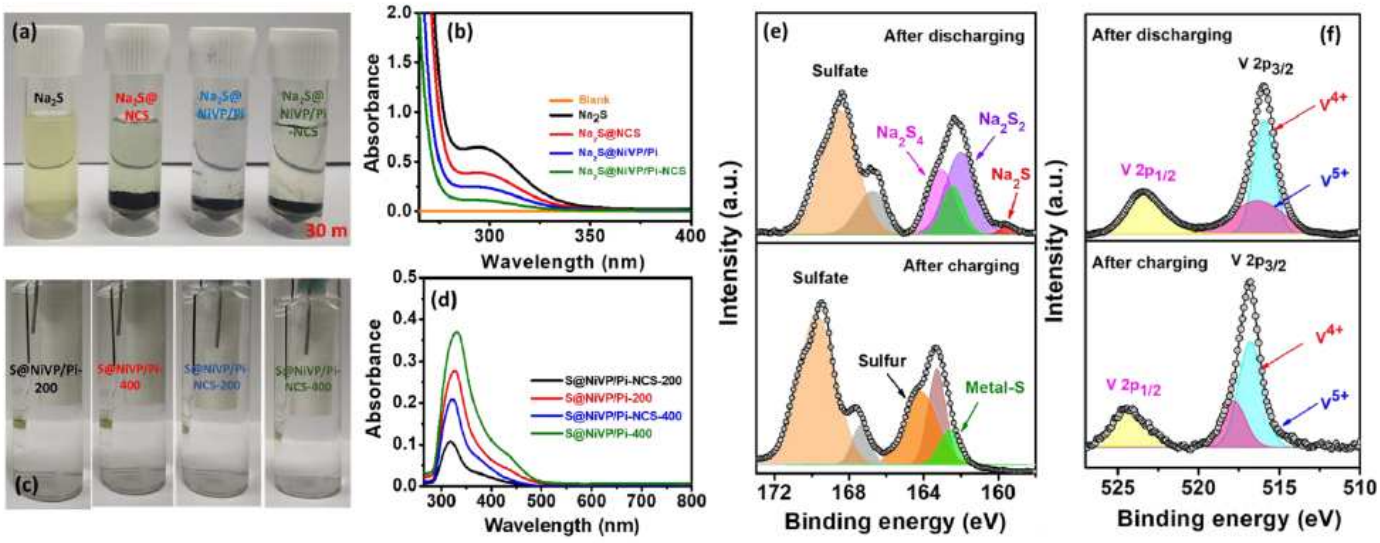

Figure 4

Visual observation, UV and XPS analysis of S@NiVP/Pi-NCS after charge-discharge process (a) Photographic images of Na2S solution with various catalyst after 30 minutes, (b) corresponding UV-vis spectra of Na2S solution of fig. 4a after 30 minutes (c) photographic images of 2 M aq. Na2SO4 electrolyte with S@NiVP/Pi-NCS and S@NiVP/Pi anodes after 200 and 400 cycles, and (d) corresponding UV-vis spectra of dissolved polysulfide in 2 M aq. Na2SO4 at various cycling performance, deconvoluted XP spectra of (e) S 2p, and (f) V 2p of S@NiVP/Pi-NCS anode after charge and discharge cycles.

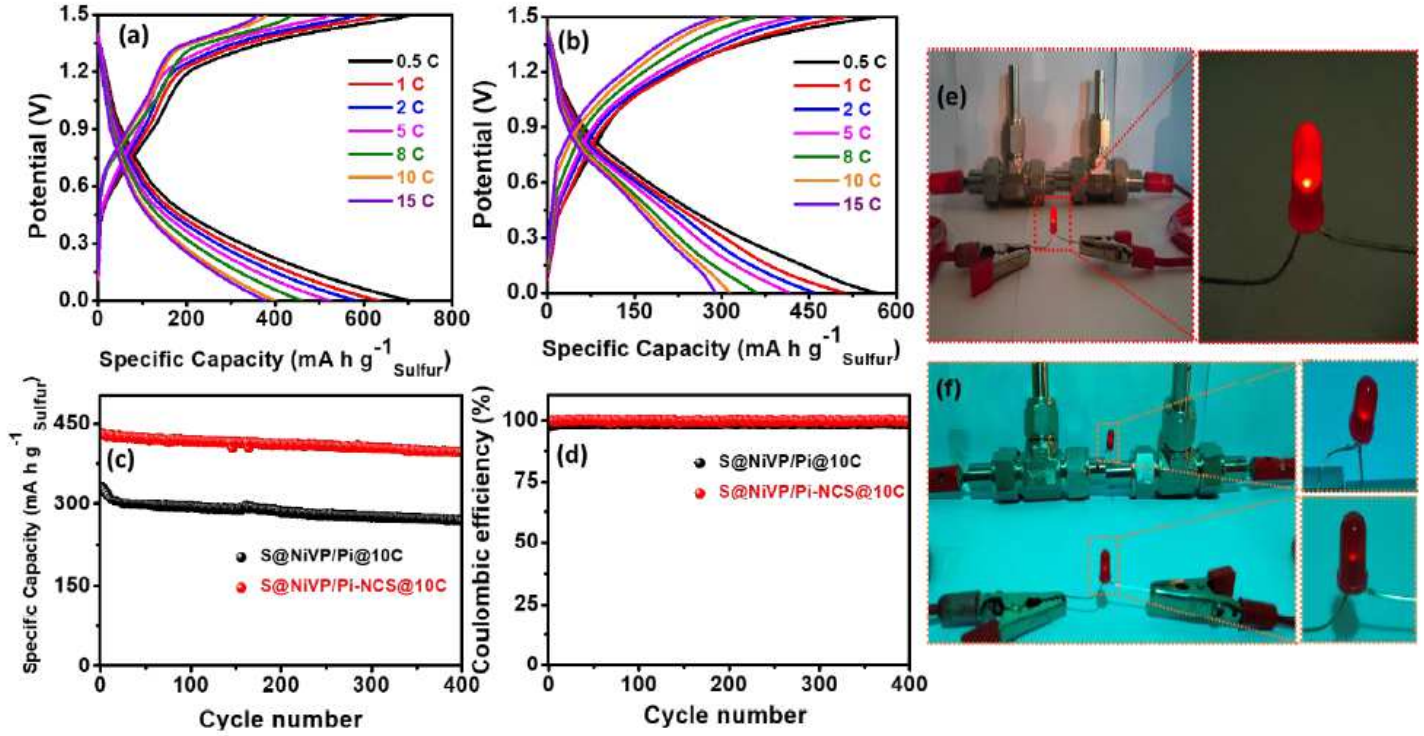

Figure 5

Full cell battery performance. Galvanostatic charge-discharge curves of full cell battery assembled using (a) S@NiVP/Pi-NCS anode + Na0.44MnO2 cathode and (b) S@NiVP/Pi anode + Na0.44MnO2 cathode at various C-rates, (c and d) corresponding battery cycling performance and coulombic efficiency at 10 C respectively over 400 cycles in 2 M aq. Na2SO4, (e), and (f) demonstration of two aqueous Na-ion/S battery consisting of S@NiVP/Pi-NCS anode and Na0.44MnO2 cathode powering LED.

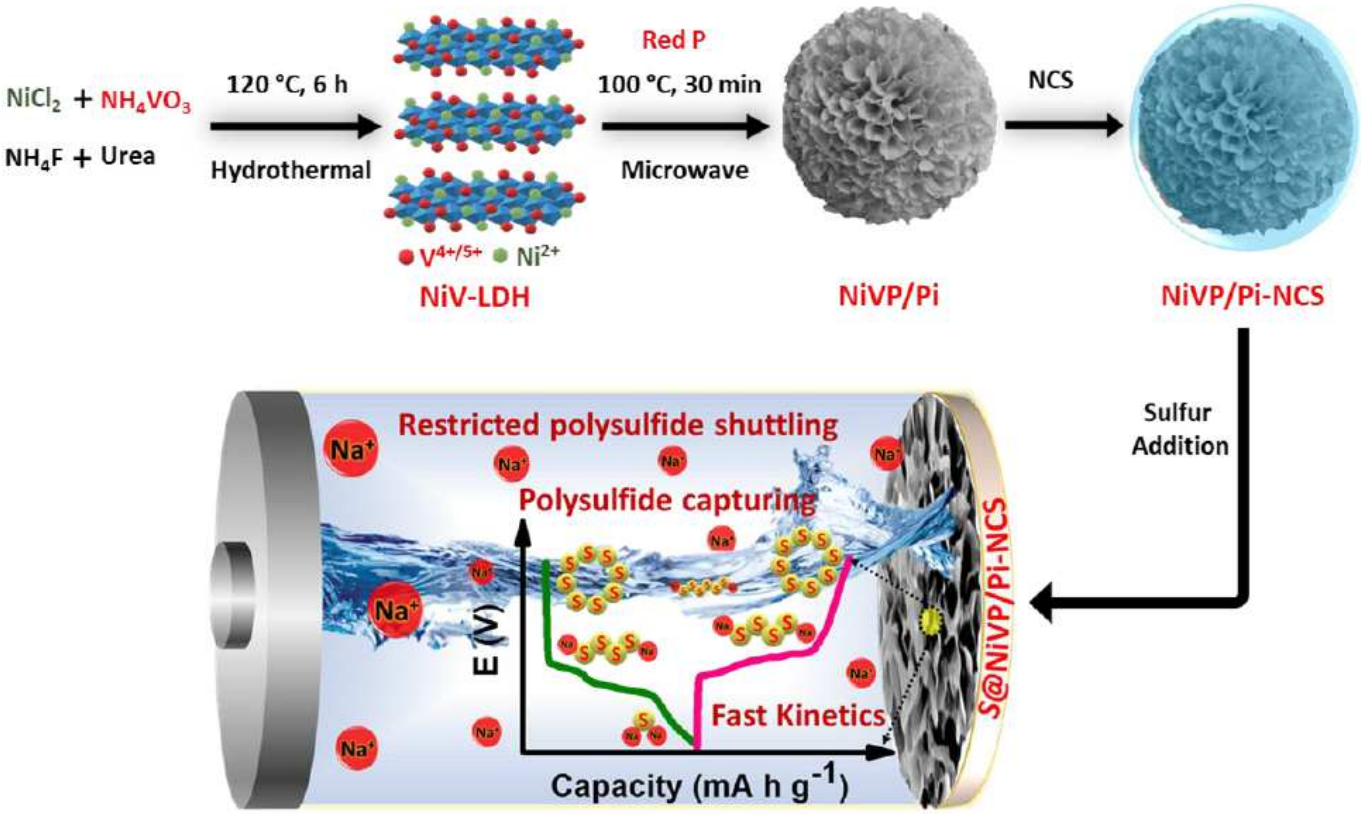

Figure 6

Scheme 1. Interaction of polysulfide @ anode. The synthetic protocol of NiVP/Pi-NCS and redox conversion of polysulfide at S@NiVP/Pi-NCS anode in aqueous Na-ion/S battery.

Supplementary Files

This is a list of supplementary files associated with this preprint. Click to download.

- 03supportinginformationaqs.NaSbatteryNiVPPPY.pdf